Discrete fracture model for simulating waterflooding processes under fracturing conditions

Gallyamov, Emil; Garipov, Timur; Voskov, Denis; Van den Hoek, Paul

DOI
10.1002/nag.2797

Publication date
2018

Document Version
Final published version

Published in
International Journal for Numerical and Analytical Methods in Geomechanics

Received: 24 November 2017 | Revised: 11 April 2018 | Accepted: 12 April 2018

DOI: 10.1002/nag.2797

RESEARCH ARTICLE

WILEY

Discrete fracture model for simulating waterflooding processes under fracturing conditions

Emil Gallyamov[1] | Timur Garipov[2] | Denis Voskov[1,2] | Paul Van den Hoek[1]

[1]Department of Civil Engineering and Geosciences, Delft University of Technology, Delft, The Netherlands

[2]Department of Energy Resources Engineering, Stanford University, Stanford, CA, USA

Correspondence
Timur Garipov, Green Earth Sciences Bldg. Rm 50, 367 Panama Street, Stanford, CA 94305, USA.
Email: tgaripov@stanford.edu

Denis Voskov, Department of Geoscience and Engineering, Stevinweg 1, 2628 CN Delft, The Netherlands.
Email: D.V.Voskov@tudelft.nl

Summary

In our study, we develop a model for simulating fracturing processes in a poroelastic medium. The proposed approach combines the discrete fracture model enriched with contact plane mechanics. The model captures mechanical interactions of fractures and a deformable medium, fluid, and heat transfer in fractures and in a porous medium. Both effects of poroelasticity and thermoelasticity are accounted in our model. Mass and heat conservation equations are approximated by the finite volume method, and mechanical equilibrium equations are discretized by means of the Galerkin finite element approach. Two-dimensional grid facets between 3-dimensional finite elements are considered as possible fracture surfaces. Most of these facets are inactive from the beginning and are activated throughout the simulation. A fracture propagation criterion, based on Irwin's approach, is verified on each nonlinear iteration. When the criterion is satisfied, additional contact elements are added into finite element and discrete fracture model formulations respectively. The proposed approach allows modeling of existing natural and artificially created fractures within one framework. The model is tested on single- and multiple-phase fluid flow examples for both isothermal and thermal conditions and verified against existing semianalytical solutions. The applicability of the approach is demonstrated on an example of practical interests where a sector model of an oil reservoir is simulated with different injection and production regimes.

KEYWORDS

discrete fracture model, fracture mechanics, geomechanics, reservoir simulation

1 | INTRODUCTION

There are certain technological operations where injection of various fluids into a subsurface is exploited. Fields, where these activities are routinely performed, comprise extraction of geothermal energy, development of unconventional hydrocarbon reservoirs, disposal of wastewater, sequestration of CO_2, storage of natural gas, and improved oil recovery. Injection of gases and liquids into subsurface formations leads to changes in their pressure, temperature, and stress state. All these phenomena can potentially lead to generation of induced fractures or activation of existing natural fractures and faults. To produce energy from the subsurface or store highly pressurized fluids underground and perform it in an efficient and safe manner, a study of fractures and faults behavior is essential.

To model hydraulically stimulated fractures, analytical and numerical models are usually used. There are a number of analytical solutions for a single fracture in a homogeneous continuous medium subjected to a uniform stress field.

Two of the most common two-dimensional (2-D) models used in fracture treatment design are Khristianovich-Geertsma-de Klerk[1,2] and Perkins-Kern-Nordgren[3,4] models. Their solutions are applicable for fractures induced in low-permeability reservoirs. There, the effect of the pressure field alteration around the fracture can be disregarded.

For different operations, such as waterflooding and water disposal processes, thermally induced fractures and poroelastic and thermoelastic stress changes cannot be ignored since fluids are injected during long periods, which is enough for them to penetrate deeply into a formation. Fracture growth happens much slower than in the case of hydraulically stimulated fractures. Analytical solutions for these problems were derived and further developed by Hagoort,[5] Koning,[6] and Van den Hoek.[7]

A number of numerical models were developed in the past to address the fracturing process. One of the approach is to couple a numerical reservoir simulator with analytical 2-D and pseudo–three-dimensional (pseudo–3-D) fracture solutions. Such models were developed and tested by Hustedt et al[8] and Dikken and Niko.[9] Another approach uses a full numerical representation of fractures and a surrounding porous medium. These models are challenging to develop because fluid flow, fracture deformation, and stress distribution have to be considered simultaneously. Some authors used the finite volume approach to model multiphase flow within a fractured medium.[10-12] Others used finite element,[13,14] mixed finite element,[14-16] and discontinuous Galerkin methods.[17,18] In addition, Faivre et al[19] considered an extended finite element formulation for coupled fluid flow and deformation of a fractured solid porous matrix. Recently, Nordbotten[20] proposed a finite volume method, and McClure and Horne[21] and Norbeck et al[22] presented a finite volume and boundary element framework for modeling coupled flow and mechanics. In most of these approaches, fractures were present in both flow and mechanical domains using simplified assumptions.

In this study, we focus on an explicit fracture approximation where fracture topology can be considered as 2 surfaces in contact. Contact mechanics was extensively studied by means of finite elements,[23] extended finite elements,[24,25] and mortar methods.[26] There are several commonly used approaches to model contact mechanics problems. They include Lagrange multipliers,[23] a penalty regularization,[27] and the Nitsche method.[28] For situations of complex fracture network topologies, where discontinuous fracture representation can be complicated, the diffusive fracture models were introduced by the continuum damage approach,[29] the phase field approach,[30,31] and level set models.[32]

The discrete fracture model (DFM), developed by Karimi-Fard et al[12] for simulating fluid flow in fractured formations, is the basis of our study. This model allows for accurate representation of pressure, temperature, and fluid distributions since all fractures are treated explicitly. However, the original method does not take into account poroelastic and thermoelastic deformations induced by injection or production. As shown by Bandis et al,[33] the hydraulic characteristics of fractures are strongly coupled to their mechanical properties, such as roughness and strength. This issue was resolved by Garipov et al,[34] where DFM was extended to account for deformations. The extended DFM inherits all the benefits of the original model and allows representation of fracture properties, such as acting stresses, conductivity, and aperture changes due to loading conditions. The extended model enables the simulation of hydromechanical behaviors of existing and nonpropagating fractures as well as faults on a large scale. However, propagation mechanisms were not addressed in the extended DFM.

In this work, we further develop the DFM approach and present a model that enables modeling of both stationary and growing fractures within the same numerical framework. The model is implemented in the Automatic Differentiation General Purpose Research Simulator (AD-GPRS) developed at Stanford University.[35] Our approach is validated against test cases with available analytical solutions. We also demonstrate applicability of the model to problems of practical interest and consider a waterflooding process, where both growing and existing fractures are modeled.

2 | THEORETICAL BACKGROUND

We consider a fractured medium as an aggregate of two objects, namely, porous medium and fractures, and accordingly introduce governing equations for both objects. The behavior of the porous medium is described by the Biot theory,[36] and fractures are considered as two surfaces in contact. Since the Biot theory is well known[37,38] and similar approaches for fractures are widely used,[34,39,40] we provide only a general description, necessary definitions, and governing equations.

2.1 | Porous medium

The porous medium is treated as a superimposition of two continua, the skeleton and the fluid.[37] Further, we consider a fluid consisting of 2 phases (compressible water and oil) and accept the following mass conservation equations:

$$\frac{\partial}{\partial t}\left(\phi\rho_j s_j\right) + \nabla\cdot\left(\rho_j \mathbf{v}_j\right) = 0, \quad j = (\mathrm{w},\ \mathrm{o}), \tag{1}$$

$$\mathbf{v}_j = -\mathbf{k}\frac{k_{rj}}{\mu_j}\nabla p_j, \tag{2}$$

$$\sum_j s_j = 1, \tag{3}$$

where (w, o) are the water and oil phases, respectively; p_j is the pressure of phase j; ρ_j and μ_j are the density and the viscosity of the phase j, respectively; k_{rj} is the relative permeability of the phase j; $\mathbf{v}_j$ is the phase velocity vector; and s_j is the corresponding phase saturation. The value ϕ is the porosity of the medium, and $\mathbf{k}$ is the permeability tensor. Further, we assume thermal equilibrium between the fluid and the solid skeleton and obtain

$$\frac{\partial}{\partial t}\left((\rho C)_{\mathrm{m}}(T-T_0)\right) + \nabla\cdot\left(\sum_j h_j\rho_j\mathbf{v}_j\right) - \nabla\cdot(\kappa_{\mathrm{m}}\nabla T) = 0, \tag{4}$$

where T is the temperature, T_0 is the reference temperature, and h_j is the enthalpy of the phase j. The medium heat capacity, $(\rho C)_m$, and the thermal conductivity of the saturated porous medium, κ_m, are defined as

$$(\rho C)_{\mathrm{m}} = \phi\sum_j C_{v,j}\rho_j s_j + (1-\phi)C_{v,\mathrm{s}}\rho_{\mathrm{s}} \tag{6}$$

$$\kappa_{\mathrm{m}} = \phi\sum_j K_j s_j + (1-\phi)K_{\mathrm{s}}, \tag{7}$$

where $C_{v,j}$ and $C_{v,\mathrm{s}}$ are the fluid phases and the skeleton-specific heat capacities, respectively; K_j and K_{s} are the thermal conductivity of the fluid phases and the skeleton, respectively; and ρ_{s} is the skeleton density. In this paper, we accept a simplified fluid description and define the fluid enthalpy and density as follows:

$$h_j = C_{v,j}(T-T_0), \tag{8}$$

$$\rho_j = \rho_{j,0} + C_{p,j}(p-p_0) - \beta_{T,j}(T-T_0), \tag{9}$$

where $\rho_{j,0}$ is the reference density and $C_{p,j}$ and $\beta_{T,j}$ are the fluid j compressibility and volumetric thermal expansion, respectively.

Changes in deformations, temperature, and pressure trigger the porosity (void space) change. In accordance with Coussy,[37] porosity update accounting for poroelastic and thermoelastic effects has the form

$$\phi = \phi_0 + \alpha\epsilon_v + \frac{(\alpha-\phi_0)(1-\alpha)}{K_{\mathrm{d}}}(p-p_0) - 3\beta_\phi(T-T_0), \tag{10}$$

where K_{d} is the drained bulk modulus, α is the Biot coefficient, $\epsilon_v = \mathrm{trace}(\epsilon)$ is the volumetric strain, and ϕ_0 is the reference porosity. Here, we define the porosity-related linear thermal expansion coefficient that can be estimated as $\beta_\phi = \beta(\alpha-\phi_0)$, where β is the linear thermal expansion coefficient.

Following Coussy,[37] we use the momentum conservation equation to describe porous medium deformation:

$$\nabla \cdot \boldsymbol{\sigma} = 0, \tag{11}$$

where the total stress tensor, $\boldsymbol{\sigma}$, accounts for contribution of both the fluid and the skeleton:

$$\boldsymbol{\sigma} = \mathbb{C}\boldsymbol{\epsilon} - \alpha \mathbf{I} p - \beta \mathbb{C} \mathbf{I} T. \tag{12}$$

Here, $\mathbf{I}$ is the identity matrix, and $\mathbb{C}$ is the elastic moduli tensor. With the adoption of the infinitesimal strain theory, the strain tensor, $\boldsymbol{\epsilon}$, can be expressed through the displacement vector, $\mathbf{u}$, as follows:

$$\boldsymbol{\epsilon} = \frac{1}{2}(\nabla \mathbf{u} + \nabla^T \mathbf{u}). \tag{13}$$

The governing equations (1, 4, and 11), in conjunction with Equations 6 and 10 and fluid properties, provide a mathematical formulation of thermo-poroelastic behavior of the saturated porous medium.

2.2 | Treatment of fractures

We represent fractures as two interfering surfaces (Figure 1). When they are in contact, we assume that a fracture is closed; otherwise, it is open. Then, we define a gap function, $g = (g_N, g_T)$, where g_N is the normal displacement relative to the reference state and g_T is the displacement in the fracture plane, as shown in Figure 1. When a fracture is open, a normal gap is negative $g_N < 0$, and $g_N = 0$ when it is closed. Surfaces of natural fractures have a rough structure that makes it possible to contain a fluid in between, for both open and closed states.

Further, we adopt the formulation given for the porous medium yet use unit porosity for fractures. Because of the nature of hydraulic properties of fractures, their hydraulic permeability, $\mathbf{k}_f$, depends on stresses acting on their surfaces when $g_N = 0$,[41] and the permeability, $\mathbf{k}_f$, becomes a function of a fracture opening when $g_N < 0$.

Stresses on surfaces are transferred by fluid and a contact. Introducing the traction vector, $\boldsymbol{t_F}(t_N, t_T)$, and projecting the total stress tensor, $\boldsymbol{\sigma}$, on a fracture surface yield

$$\boldsymbol{t_F} = -\boldsymbol{\sigma}\boldsymbol{n} = -(\boldsymbol{\sigma}' - \mathbf{I}p)\boldsymbol{n} = t_N \boldsymbol{n} + t_T \boldsymbol{\tau} + p\mathbf{I}\boldsymbol{n}, \tag{14}$$

where $\boldsymbol{n}$ and $\boldsymbol{\tau}$ are the normal and tangential unit vectors, defined on each fracture surface, and $\boldsymbol{\sigma}'$ is the effective stress. Here, we also assume continuity of all the components of $\boldsymbol{t_F}$ across fracture surfaces. For open fractures, components t_N are t_T are vanishing, and only pressure p holds apart fracture faces. Further, we distinguish two states of closed fractures, namely, slip and stick:

$$t_N = 0 \text{ and } g_N < 0, \quad \text{open fracture} \tag{15}$$

$$t_T < \mathcal{F}(t_N),\ \dot{g}_T = 0, \text{ and } g_N = 0, \quad \text{stick state} \tag{16}$$

$$t_T = \mathcal{F}(t_N),\ \dot{g}_T > 0, \text{ and } g_N = 0, \quad \text{slip state}. \tag{17}$$

Here, the dot denotes a derivative of the gap function with respect to time, ie, the deformation rate or change in gap between loading steps. The slip state is possible when the tangential and normal components are coupled by the friction law $\mathcal{F}$.

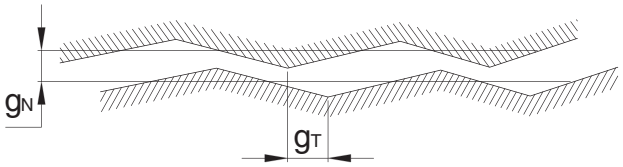

FIGURE 1 Illustration of a fracture

In this study, we consider brittle materials and use Irwin's criterion for linear elastic failure[42]:

$$K_{\mathrm{I}} \leq K_{\mathrm{Ic}}. \tag{18}$$

Fracturing occurs when a fracture Stress Intensity Factor (SIF), K_{I}, reaches a fracture toughness value, K_{Ic}. A fracture grows toward a plane with maximum tangential tensional effective stress.

3 | SOLUTION METHOD

3.1 | Domain discretization

In this section, we discuss a discretization of the governing equations. Figure 2(A) shows a physical domain, Ω, where the external contour of the model is defined by Γ and the fracture surfaces are defined by Γ_f. Figure 2(B) gives an example of discretization of the matrix using triangles (wedges, tetrahedrons, and hexahedrons in 3-D) and the fracture using segments (thick lines). This geometrical grid is used for both flow and mechanical problems. For the flow/energy equations, we associate control volumes with every element of the grid, as shown in Figure 2(B). Then, we define piecewise constant primary variables, such as pressure and temperature, at each control volume. For mechanics, fractures are delineated as contacts between matrix elements. We define primary variables, $\mathbf{u}$, at vertices and secondary variables, traction vectors, $\boldsymbol{t_F}$, on fracture surfaces. Their locations correspond to the Gauss points used for numerical integration. Discretization of the mechanical domain is given in Figure 2(C).

The flow/heat equations are discretized using a finite volume technique with a two-point flux approximation. Following Karimi-Fard et al,[12] the flow/heat rate between two adjacent control volumes is expressed through pressure and temperature gradients. The mechanical equations use the standard finite element approximation. In addition to that, contacting elements (triangles and quads in 3-D) have associated contact forces. Calculation of these forces is based on the "penalty" approach, when a force is proportional to the penetration of one element into another.[43]

In this study, we discuss modifications of a discretization scheme for the geomechanical part only, since we use existing capabilities of the research simulator AD-GPRS developed at Stanford University. The simulator allows us to solve the variety of multiphysics problems including coupled thermal-compositional flow[44] and geomechanics.[45] The details of approximation techniques of the mass and energy conservation equations can be found in previous works.[12,46-48]

An illustration of the numerical treatment of fractures is given in Figure 3. Here, we define a contact element as "master" and "slave" faces in contact, and a vector, $\mathbf{t}_F$, is defined at each Gauss integration point on the master surface. When a failure criterion is satisfied, the fracture propagates one element further from its tip. Next, we separate two cells, create a new pair of the master and slave faces, and add a new set of vertices. The grid, used to discretize mass and energy balance equations, is not affected by this procedure since it already has finite volumes assigned to every possible fracture geometry.

3.2 | Discretized governing equations

The DFM was extensively used to discretize the mass and energy balance equations by many authors.[10-12] Thus, we only focus on the treatment of the mechanics equations and introduce a weak form of Equation (11):

$$\int_{\Omega} \delta\boldsymbol{\epsilon}:\boldsymbol{\sigma} d\Omega - \int_{\Gamma} \delta \boldsymbol{u} \boldsymbol{t} d\Gamma - \int_{\Gamma_f} \delta g_N p_f d\Gamma_f - \int_{\Gamma_f} (\delta g_N t_N + \delta g_T t_T) d\Gamma_{\mathrm{f}} = 0. \tag{19}$$

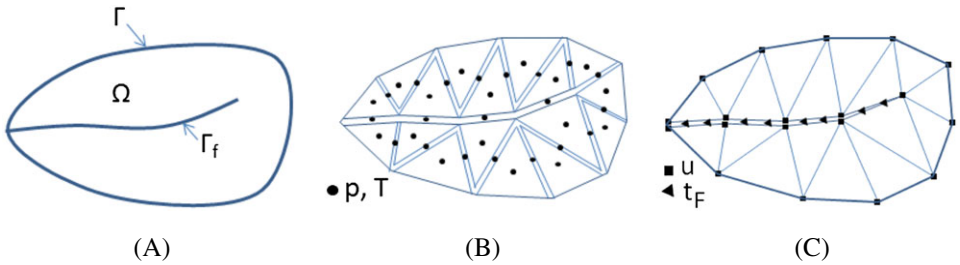

FIGURE 2 Illustration of a grid structure. A, Physical domain, Ω, and external, Γ, and internal, Γ_f, boundaries. B, Extended grid for flow with variables defined in cell centers. C, Grid for mechanics with variables assigned in cell vertices and contact surfaces [Colour figure can be viewed at wileyonlinelibrary.com]

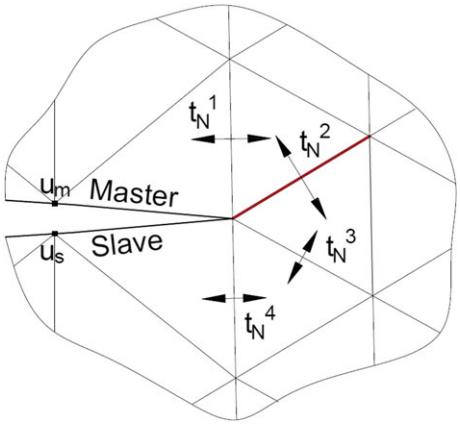

FIGURE 3 Illustration of the numerical treatment of a fracture. Its surfaces are labeled as "master" and "slave." The fracture propagates along a plane with maximum tangential tensional effective stress [Colour figure can be viewed at wileyonlinelibrary.com]

Here, t_N and t_T are the normal and tangential components of a traction vector $\boldsymbol{t_F}$ acting on a boundary Γ_f, values g_N and g_T are the normal and tangential components of a fracture gap function, p_f is the pressure inside the fracture, $\boldsymbol{t}$ is the traction vector acting on the external boundary Γ. The gap function components are equal to $g_N = (\boldsymbol{u}_m - \boldsymbol{u}_s)\boldsymbol{n}$ and $g_T = (\boldsymbol{u}_m - \mathbf{u}_s)\boldsymbol{\tau}$, where vectors $\boldsymbol{u}_m$ and $\boldsymbol{u}_s$ are the displacement vectors on the master and slave faces correspondingly. It is important to mention that the last term in Equation 19 is present only when the fracture is closed and the two surfaces of it are in contact. As soon as it opens, the contact integral vanishes:

$$\int_{\Gamma_f} (\delta g_N t_N + \delta g_T t_T) d\Gamma_f = 0. \tag{20}$$

For the open fracture, the only force acting on a contact Γ_f is the pressure p_f. This situation is common for growing fractures. However, treatment of the integral in Equation 20 becomes important when a previously growing fracture closes or some preexisting fractures are present.

The traction vector $\boldsymbol{t_F}(t_N, t_T)$ is defined at the Gauss integration points and is evaluated using the return mapping algorithm:

$$\begin{gathered}\text{Compute gap function} (g_N, g_T)^{n+1} \text{at the Gauss integration point.} \\ \text{Evaluate the normal traction :} \\ t_N^{n+1} = \varepsilon_N g_N^{n+1}.\end{gathered} \tag{21a}$$

$$\begin{gathered}\text{Compute a trial tangential traction predictor and evaluate the yield function :} \\ t_T^{\text{trial}} = t_T^n + \varepsilon_T \left(g_T^{n+1} - g_T^n\right) = \varepsilon_T \left(g_T^{n+1} - g_T^{p,n}\right),\end{gathered} \tag{21b}$$

$$\Phi^{\text{trial}} = \left|t_T^{\text{trial}}\right| - \mathcal{F}\left(t_N^{n+1}\right). \tag{21c}$$

$$\begin{gathered}\text{If the yield condition, } \Phi^{\text{trial}} \leq 0, \text{ is satisfied, then set} \\ t_T^{n+1} = t_T^{\text{trial}}.\end{gathered} \tag{21d}$$

$$\begin{gathered}\text{Else iterate } \left(t_T^{n+1}, \Delta\lambda\right): \\ g_T^{p,n+1} - g_T^{p,n} - \Delta\lambda \frac{\partial \Phi}{\partial t_T} = 0,\end{gathered} \tag{21e}$$

$$\Phi = \left|t_T^{n+1}\right| - \mathcal{F}\left(t_N^{n+1}\right) = 0. \tag{21f}$$

$$\text{Here, } t_T^{n+1} - \varepsilon_T \left(g_T^{n+1} - g_T^{p,n+1}\right) = 0. \tag{21g}$$

Here, the indices $(n+1)$ and (n) refer to the current and previous time steps, respectively, $\Delta\lambda$ is the plastic multiplier, and g_{T}^{p} is the irrecoverable tangential slip. The iterative procedure (21e-21f) are similar to the return mapping algorithm considered in other studies.[49,50]

3.3 | Evaluation of the SIF

We use the SIF K_{I} as a fracture propagation criterion. There are a number of methods used in fracture mechanics to evaluate K_{I}. Simulations at the reservoir scale demand that the K_{I} calculation procedure could be performed on a reasonably coarse mesh with an acceptable accuracy.

The plain strain analytical solution for a local displacement field near a fracture tip couples material properties and the SIF:

$$\begin{aligned} u_x &= \frac{K_{\mathrm{I}}}{G}\sqrt{\frac{r}{2\pi}}\cos(\theta/2)[1-2\nu+\sin^2(\theta/2)], \\ u_y &= \frac{K_{\mathrm{I}}}{G}\sqrt{\frac{r}{2\pi}}\sin(\theta/2)[2-2\nu-\cos^2(\theta/2)], \end{aligned} \tag{22}$$

where G is the shear modulus, r is the distance from the fracture tip, ν is the Poisson ratio, and θ is the angle estimated from the plane in front of the fracture tip. Inverting (22) for K_{I} and taking $\theta=\pi$, such that displacements along the fracture surface are evaluated, yield an expression for K_{I}. Applying a similar procedure on the set of equations written in terms of K_{II} yields an expression for K_{II}:

$$\begin{aligned} K_{\mathrm{I}} &= \sqrt{\frac{2\pi}{r}}\frac{Gu_y}{2(1-\nu)}, \\ K_{\mathrm{II}} &= \sqrt{\frac{2\pi}{r}}\frac{Gu_x}{2(1-\nu)}. \end{aligned} \tag{23}$$

The proposed formulas cannot be directly used in numerical implementation since an exact value of K_{I} and K_{II} is undefined when r is 0. Therefore, an estimation of SIFs from the closest to the tip element would give an erroneous number. To directly use a definition of SIF, Fu et al[51] suggested an empirical procedure to calculate a correction factor based on a mesh topology and an element size. The procedure directly applies the analytical expression to calculate SIF at the element connected to the fracture tip yet multiplies the calculated value by a correction value to eliminate the numerical error. Chan et al[52] proposed the Displacement Extrapolation Technique (DET), where values of K_{I}^{*} are approximated at some distance r from the fracture tip inwards the fracture. Then, a range of K_{I}^{*} values, not affected by the tip interference, is identified. A final value of K_{I} is then obtained by extrapolating the K_{I}^{*} toward the fracture tip based on the previously defined range. The DET is schematically shown in Figure 4.

The described algorithm perfectly works for 2-D straight fractures. However, its 3-D extension is not trivial. An alternative algorithm is based on the Virtual Crack Closure Technique method. This method uses only local information near the fracture tip and is suitable for 3-D simulations.[53] The method is based on the energy balance proposed by Irwin, and its extensive overview and calculation procedures are performed by Krueger.[54] For testing purposes, both methods were implemented and tested in our numerical framework.

3.4 | Solution algorithm

The solution procedure, presented in this section, contains several key steps. First, we solve the mass, energy, and momentum balance equations using the Newton iterations. On each iteration, we evaluate the SIF at the fracture tip. Finally, we update the fracture trajectory and mesh parameters if it is necessary and continue iterations. In this procedure, we consider a single growing fracture Γ_{f^a} and closed fractures Γ_{f^p}. We directly apply the return mapping algorithm equations (21a-21f) to evaluate stress values on the closed fractures. We assume that Γ_{f^a} extends from its tip, and branching is not allowed. If the fracturing condition is satisfied, then the selected face is added into Γ_{f^a}, and it obtains a new status. The fracture status allows us to distinguish active fracture faces (all the faces on fracture surfaces Γ_{f^a}), assign a conductivity calculation law, and track its trajectory.

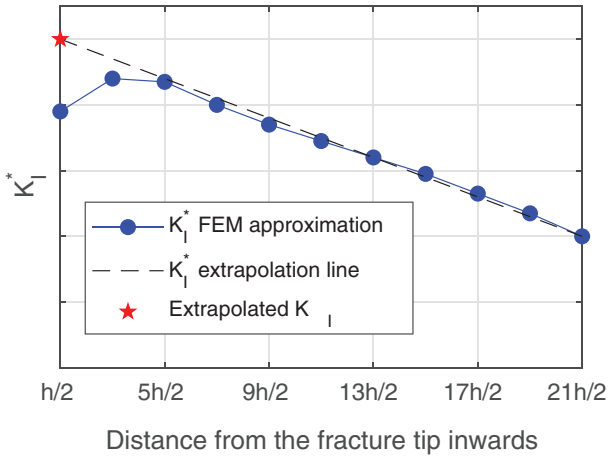

FIGURE 4 Illustration of the Displacement Extrapolation Technique. K_I^* are evaluated at the centers of the fracture segments. Left extreme of the plot is the center of the element closest to the fracture tip. Distance inwards the fracture increases from left to right [Colour figure can be viewed at wileyonlinelibrary.com]

The details of the algorithm are given in Appendix B. The proposed algorithm requires modification of an existing nonlinear procedure for the solution of an extended DFM model[34] and includes detection of opening and closing events of the growing fracture, an additional procedure for pressure stabilization on nonlinear iterations, and an adjusted convergence criterion. It is necessary to mention that the developed algorithm works for closed fractures without limitation yet demands one growing fracture that does not intersect other fractures. The approach can be extended for multiple growing fractures; however, modeling of interaction between them still requires additional efforts.

4 | MODEL VALIDATION

In this section, we validate the developed framework against a semianalytical solution proposed by Koning.[6] We consider several test cases, which include different types of injection scenarios. First, we test a scenario where injected and reservoir fluids have the same properties. Second, we consider injection of water into a reservoir containing oil, which is the most common scenario in practice. It is distinguished by the development of a separation interface between two fluids known as a waterfront. This example contains favorable (sharp waterfront) and unfavorable (smeared front) types of displacement. Third, we study how temperature of an injected fluid affects fracture evolution. Finally, we investigate the effects of mesh resolution, time step size, and mesh irregularity along the fracture path.

Koning[6] considered a simplified formulation for a decoupled problem and used a total compressibility of the porous medium. To satisfy the Koning formulation, we consider incompressible fluids for all the test cases and use the following equation for porosity change:

$$\phi = \phi_0 + C_{p,r}(p - p_0) - \beta_{T,r}(T - T_0), \tag{23}$$

where $C_{p,r}$ and $\beta_{T,r}$ are the rock compressibility and volumetric rock thermal expansion coefficient.

4.1 | Model geometry, boundary, and initial conditions

The considered model contains a reservoir with an initial fracture. We simulate only half of the domain because of a given symmetry of the problem. The model size is 300 m in the Y direction and 150 m in the X direction. The corresponding unstructured grid is shown in Figure 5(C). This grid has a predefined fracture propagation line and a refinement along it.

The reservoir is modeled as a 3-D plate with a unit thickness. The illustration of the domain size and boundary conditions for a flow problem can be seen in Figure 5(A). We apply no flow boundary conditions on the left side of the model and a constant pressure value p_r at the radius R_r. The initial reservoir pressure equals p_{init}.

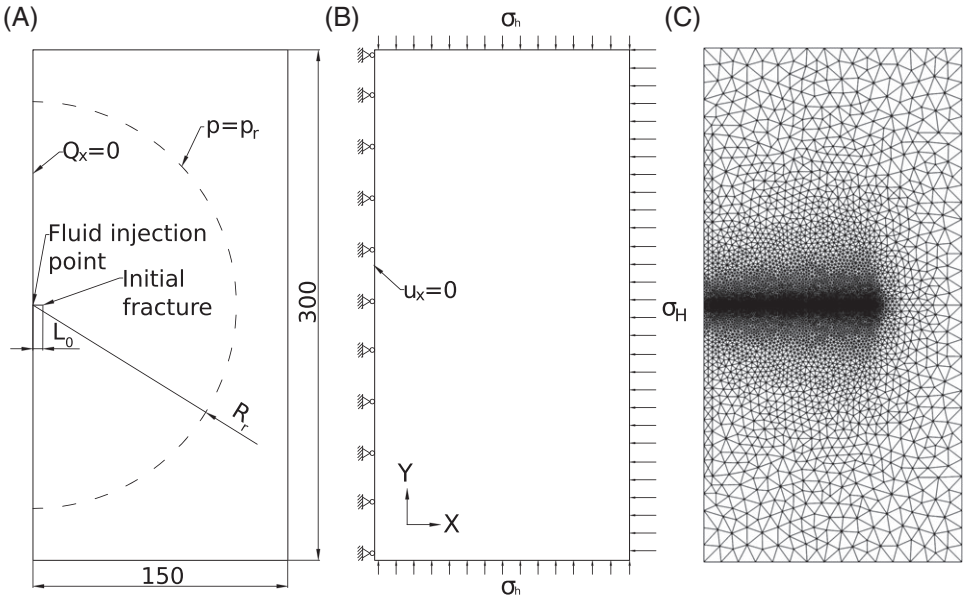

FIGURE 5 The model used for simulations. Flow (A) and mechanics (B) problems boundary and initial conditions. C, Unstructured grid

A schematic view of mechanical boundary conditions is given in Figure 5(B). The upper and lower boundaries are loaded by the stress σ_h, and the right boundary is loaded by σ_H. The initial conditions for the mechanical problem are defined by the stress state, which complies with the boundary conditions (σ_h and σ_H). The symmetry condition for mechanics is applied by fixing displacements in the X direction on the left boundary. To exclude the rigid body motion, we fix a single-node displacement in the Y direction.

Fluid is injected into the existing fracture with the initial length L_0 under a constant rate Q. This leads to accumulation of pressure and following fracture extension. Analytical derivation of the solution is given in Appendix A and is used for validation of numerical results.

4.2 | Single-phase fluid flow

First, we consider a fracture growing due to injection of a single-phase fluid (water) into the reservoir. Properties of the porous medium, fluid, and fracture, used in the current model, are given in Table 1. The pressure profile across the domain in the beginning and the end of propagation is shown in Figure 6.

Development of the fracture length and pressure inside the fracture as function of time can be seen in Figure 7. Numerical fracture length, given in Figure 7(A), has a good match with the analytical solution. Both curves coincide in terms of fracture initiation time and its length during the growth stage. When the pressure front reaches the pressure boundary, the analytical curve flattens ($t > 6{\cdot}10^{-2}$day). The difference between the final length in the numerical and analytical solutions is caused by certain simplifications used in the semianalytical solution. Indeed, the solution given by Koning[6] assumes constant reservoir pressure after the pressure wave reaches the boundary. In contrast, the numerical model captures the effect of further pressure change, and, consequently, the fracture keeps growing. When the pressure solution becomes stationary ($t > 1{\cdot}10^{-1}$ day), fracture growth stops. Nevertheless, the numerical solution fairly reproduces the analytical solution within its applicability range.

Pressure, normalized over minimum horizontal stress σ_h, is given in Figure 7(B). There is a close fit between two curves in the validity range of the analytical solution. During the initial pressure buildup ($t < 4{\cdot}10^{-3}$day), pressure in the fracture accumulates above the sum of minimum horizontal stress σ_h and pressure-induced stress $\Delta\sigma_p$. Less pressure is needed for the fracture to grow when it becomes longer (see Appendix A).

It is important to point that normalized pressure is always higher than one or higher than the initial stress σ_h, which indicates a buildup of pressure-induced stresses $\Delta\sigma_p$ (see Figure 7B). Similar observations were obtained by Carrier and Granet[55] and Salimzadeh et al.[56] These authors demonstrated the important impact of pressure-induced stresses on the dynamics of growing fractures.

TABLE 1 Properties used in the single-phase simulation

Property	Value
Reservoir drainage radius R_r, m	100
Initial fracture length L_0, m	5
Stress in the X direction σ_H, MPa	−30
Stress in the Y direction σ_h, MPa	−25
Initial reservoir pressure p_{init}, MPa	18
Reservoir pressure at the drainage radius p_r, MPa	18
Porosity ϕ	0.3
Permeability k, mD	25
Fracture conductivity c_f, mD · m	∞
Biot coefficient α	1
Young modulus E, GPa	50
Poisson ratio ν	0.25
Rock compressibility $C_{p,r}$, 1/Pa	$1{\cdot}10^{-10}$
Water density ρ_w, kg/m^3	1000
Water viscosity μ_w, cP	1
Injection rate (into a half-fracture) Q, m^3/day	30

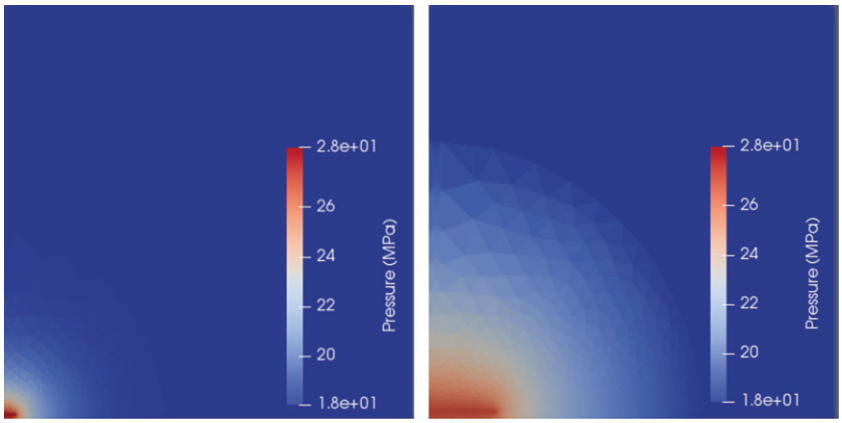

(A) (B)

FIGURE 6 Pressure profile (A) before and (B) after fracture growth [Colour figure can be viewed at wileyonlinelibrary.com]

4.3 | Favorable displacement

In this section, we consider a multiphase flow problem. In this model, we inject water into an oil-filled reservoir, which is commonly done during secondary oil recovery operations. This scenario leads to a development of a separation interface between two fluid phases (waterfront). Whether a waterfront is sharp ("favorable" or "piston-like" displacement) or smeared ("unfavorable" displacement) strongly depends on the ratio between relative mobilities of the two fluids. The adopted semianalytical solution was derived for a favorable fluid displacement and constant relative permeabilities of each phase k_{rw} and k_{ro} within flooded and displaced zones. To match the numerical and analytical solutions, we chose fluid parameters properly to approximate favorable displacement type. The fluid properties are given in Table 2. Resulting mobility ratio $M \leq 1$ allows oil to flow with the same or even higher velocity than water, which leads to the favorable displacement scenario. In contrast, mobility ratio $M \geq 1$ leads to a faster water flow. As before, we use incompressible fluids and set the rock compressibility $C_{p,r}$ equal to $1{\cdot}10^{-10}$ 1/Pa.

The numerically obtained fracture length (Figure 8A) has a perfect match with the analytical solution during primary fracture growth. At this stage, the main driver of the fracture propagation is pressure growth inside the reservoir,

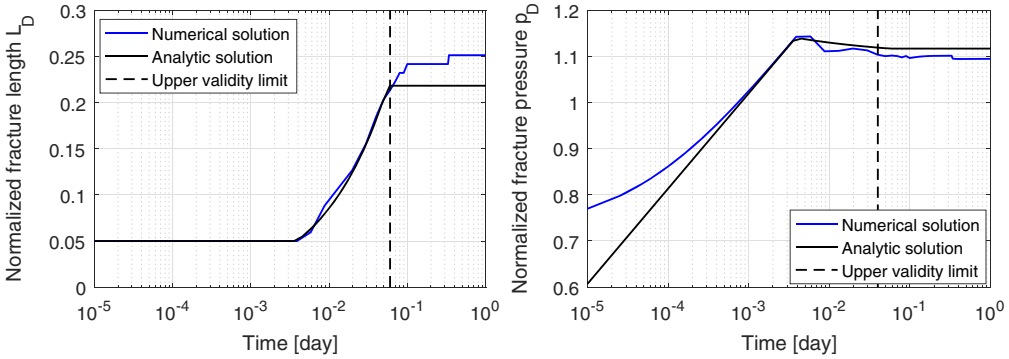

(A) (B)

FIGURE 7 Development of (A) the fracture length and (B) pressure in the numerical model compared with the semianalytical solution. The numerical model has an average mesh size equal to 1.0 m. The time step dynamically changes from $1{\cdot}10^{-5}$ to $1{\cdot}10^{-2}$ day. Results for the fracture length and pressure are normalized by the radius of the reservoir R_r and minimum horizontal stress σ_h accordingly [Colour figure can be viewed at wileyonlinelibrary.com]

TABLE 2 Properties used in multiphase simulations

	Favorable displacement		Unfavorable displacement	
Phase parameter	**IF**	**DF**	**IF**	**DF**
Viscosity μ_j, cP	0.5	1.0	0.5	1.0
Density ρ_j, kg/m^3	1000	850	1000	850
Endpoint relative permeability k_{rj}	0.3	0.7	1.0	1.0
Irreducible saturation S_i	0	0	0	0
Corey exponent	1	1	1	1
Mobility ratio M	0.85		2.0	

Abbreviations: IF, injected fluid; DF, displaced fluid.

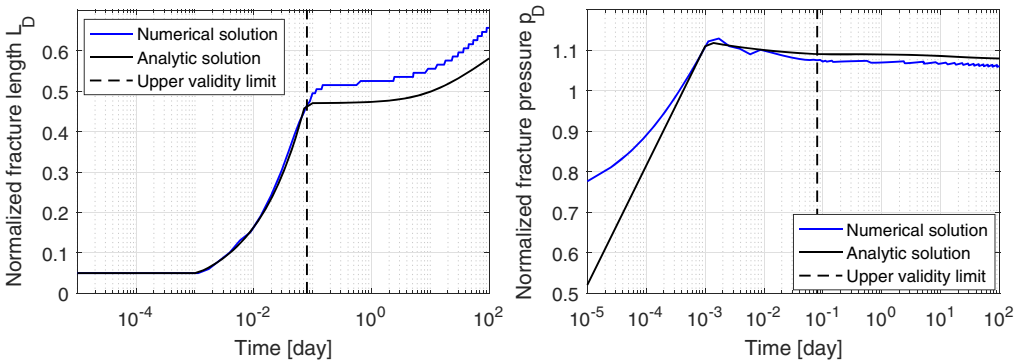

(A) (B)

FIGURE 8 A, Comparison between the numerical and analytical solutions for the fracture length normalized over the distance to the aquifer, $L_D=L/R_r$, in conditions of the favorable multiphase flow. Numerically obtained length matches the analytical solution during the primary growth stage and has the same increase rate during the secondary stage. B, Comparison between the numerical and analytical solutions for pressure normalized over minimum horizontal stress, $p_D=p/\sigma_h$. Two curves differ in the early-time stage owing to the limited validity of the analytical solution. Both solutions indicate similar fracture growth initiation time, after which pressure decreases as the fracture keeps opening [Colour figure can be viewed at wileyonlinelibrary.com]

which is almost 100% filled by oil. When a pressure signal reaches the boundary R_r, the analytical solution "freezes" (as in the previous example) while the numerical solution keeps developing, as it accounts for the residual compressibility of the fluid.

The secondary fracture growth is caused by expansion of the flooded zone. In the case of favorable displacement, the injected fluid is less mobile than the displaced one. To displace the larger volume of the less mobile fluid, the fracture has to extend. Expansion of the flooded zone leads to the further fracture growth. The rate of the secondary fracture growth is the same in the numerical and analytical solutions.

Bottom hole pressure change is shown in Figure 8(B). At the moment t=0, the normalized pressure is equal to the normalized initial reservoir pressure of 0.72 (it is normalized by the horizontal stress σ_h). This value is not shown in the figure owing to the logarithmic timescale. While two solutions differ in the early-time stage because of the limited applicability of the analytical model, there is a fair agreement in the late-time stage. It includes pressure break time due to fracture growth initiation as well as further pressure decrease due to fracture opening and growth. The pressure behavior is similar to the single-phase case.

4.4 | Unfavorable displacement

In the unfavorable displacement regime, more mobile water is injected into less mobile oil, which leads to smearing of the water saturation profile. While the piston-like displacement assumption, adopted for the analytical solution, does not hold anymore, the numerical model can realistically reproduce both the saturation front and the pressure profile of the unfavorable oil displacement.

Results of the simulation and its comparison with the analytical solution are presented in Figure 9. Primary fracture growth, shown in Figure 9(A), is caused by the initial pressure buildup across the domain. In the second stage, expansion of the zone flooded with a more mobile fluid leads to the gradual fracture closure. As a smaller fracture length is needed to displace more mobile fluid, the fracture shortens. Both the numerical and analytical curves capture this closing behavior. A moderate difference between two solutions during the initial pressure growth can be seen in Figure 9 (B). Further, the fracture starts to close because of the expansion of the flooded zone and the difference between two solutions becomes more pronounced. Both solutions qualitatively provide similar results, yet only the numerical solution is accurate since the analytical model uses simplified assumptions. This example illustrates the ability of the developed numerical model to reproduce a fracture closure phenomenon, also observed during laboratory experiments.[57,58]

4.5 | Fracture growth due to cooling

In the previous examples, the effect of temperature-induced stresses was ignored. Injected fluid had the same temperature as the reservoir. In the current section, we consider the effect of cooling. Fluid and porous skeleton parameters, used in the following test, are given in Table 3. We use the same skeleton properties as before, yet adding temperature-related parameters (see Table 3 for details). A higher rock compressibility (see Table 3) was used to delay the pressure-induced stress change and to exaggerate the thermally induced stresses. The main purpose of this section is to demonstrate the effect of the temperature-induced stresses on the fracture growing process.

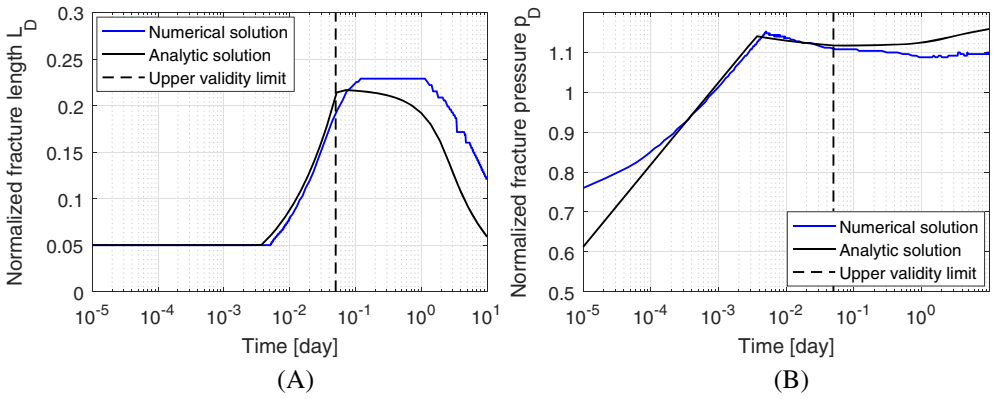

FIGURE 9 A, Comparison between the numerical and analytical solutions for the normalized fracture length, L_D=L/R_r, in conditions of unfavorable multiphase flow. Length development profiles have similar behavior during the primary and secondary stages. B, Comparison between the numerical and analytical solutions for normalized pressure, p_D=p/σ_h. Pressure profiles have similar behavior during the primary fracture growth [Colour figure can be viewed at wileyonlinelibrary.com]

TABLE 3 Properties used in the thermal simulation

Property	Value
Reservoir drainage radius R_{res}, m	100
Initial fracture length L_0, m	5
Stress in the X direction σ_H, MPa	−62
Stress in the Y direction σ_h, MPa	−57
Initial reservoir pressure p_{init}, MPa	50
Pressure on the drainage radius p_R, MPa	50
Initial reservoir temperature T_{init}, K	373.15
Rock compressibility $C_{p,r}$, 1/Pa	$1{\cdot}10^{-8}$
Rock thermal expansion $\beta_{T,r}$, 1/K	$2.1{\cdot}10^{-6}$
Specific heat capacity $C_{v,s}$, kJ/(kg K)	0.78
Thermal conductivity K_s, kJ/(m day K)	0
Fluid thermal expansion coefficient $C_{T,j}$, 1/K	0
Viscosity μ_j, cP	1
Specific heat capacity $C_{v,j}$, kJ/(kg K)	4.185
Thermal conductivity K_j, kJ/(m day K)	0
Injected fluid temperature T_{inj}, K	323.15

We apply the no-flow boundary condition on the left side of the model and the constant pressure value p_R=50 MPa at the radius R_{res}=100 m. The initial reservoir pressure is p_{init}=50MPa. The upper and lower boundaries are loaded by the stress σ_h=−57 MPa, and the right boundary is loaded by σ_H=−62 MPa. Symmetry conditions for mechanics are applied by fixing displacements in the X direction on the left boundary. For simplicity, the thermal domain has a zero-heat flow condition on its external boundaries.

As shown in Appendix A, the semianalytical solution for stresses induced by pressure and temperature is based on the assumption of a zero-heat conduction. To reproduce a similar setup in our numerical model, the thermal conductivity is taken zero for both the skeleton and the fluid. Reduction of the effective stresses, necessary for the fracture to grow, at first, happens because of the thermal contraction of the skeleton rather than high fluid pressure inside. Later, further contribution of the fracture pressure and the poroelastic effect increases and adds to the thermoelastic driver. After that, the fracture continues growing because of both pressure and temperature effects.

The analytical solution for the fracture pressure and length can be seen in Figure 10. Skeleton shrinkage due to cooling leads to a reduction of the bottom hole pressure, necessary for the fracture to grow. This effect can be clearly seen when comparing analytical pressure curves with and without temperature contribution (Figure 10B). A similar

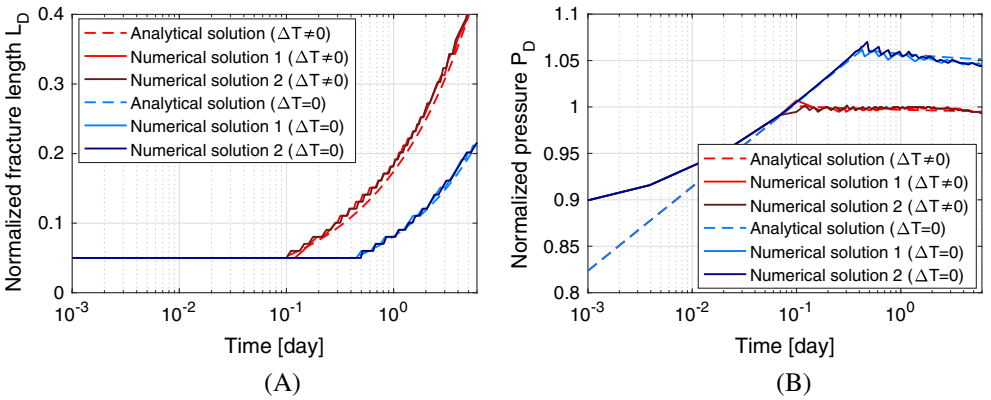

FIGURE 10 Comparison between numerical and analytical solutions of (A) normalized length, L_D=L/R_{res}, and (B) normalized pressure inside the fracture, p_D=p/σ_h, in the thermal simulation. The numerical solution 1 is obtained by the Displacement Extrapolation Technique and the numerical solution 2 by the Virtual Crack Closure Technique [Colour figure can be viewed at wileyonlinelibrary.com]

behavior can be observed in the length-vs-time plot in Figure 10(A). The "cold" fracture starts growing earlier than the isothermal one. When the latter detains, the "cold" fracture keeps growing because of the strong thermoelastic effects. The effect of thermoelasticity is particularly revealing itself in the different timing of the fracture growth initiation and is perfectly captured by the numerical model.

As discussed in Section 3.3, our numerical framework supports two methods of SIF evaluation: the Displacement Extrapolation Technique[52] and the Virtual Crack Closure Technique.[53] The first method uses a sequence of displacement values along a fracture surface and extrapolates K_I toward the fracture tip. The second method uses only local information at the tip. A comparison of results obtained using two different methods is shown in Figure 10. It demonstrates that within the developed model the Displacement Extrapolation Techinque and the Virtual Crack Closure Technique provide similar results.

4.6 | Mesh refinement study

The following step in the model verification is testing the effects of the selected model parameters on the results. Such parameters are the mesh size and the characteristic time step. Both tests are done based on the single-phase setup. Parameters are given in Table 1 unless indicated otherwise.

To evaluate the effect of the mesh size on the resulting solution, a mesh refinement study was conducted. Simulations were performed with 4 meshes. They differ in size of the elements along the fracture path. The following sizes were used: 0.25, 0.5, 1.0, and 2.0 m. The elements along the fracture path are the smallest in the whole domain. The element size gradually increases toward the boundaries of the model (see Figure 5C). The maximum size of the elements adjoining the external boundary is constant for all simulations and equals to 20.0 m. The maximum time step in this study was limited to $1{\cdot}10^{-3}$ days. Figure 11(A) shows the effect of mesh size on the fracture length. Curves obtained for the meshes with minimum sizes of 0.25 and 0.5 m are in fair agreement with each other and with the analytical curve. Results for the larger mesh sizes slightly outrun the analytical solution. This happens because the waiting time between 2 subsequent openings of larger fracture segments also becomes larger. To have a close fit between numerical and analytical solutions, the size of the elements adjoining the fracture should be kept below 1.0 m in the parameter space of the problem.

Figure 11(B) shows the variation of the bottom hole pressure for four mesh sizes. Coarser meshes display higher jumps in pressure upon the opening of each segment. For denser meshes, these jumps are less noticeable as the volume of a newly opened fracture segment that has to be filled with a fluid is smaller.

4.7 | Time step size effect

In this section, we consider the time step effect on the solution for pressure and fracture length. The following simulations were performed on the same model previously used (single-phase setup) with an average mesh size equal to 0.5 m. Every simulation is conducted with a constant time step. The range of used time steps varies between the smallest one of $1{\cdot}10^{-3}$ day and the largest one of 0.1 day.

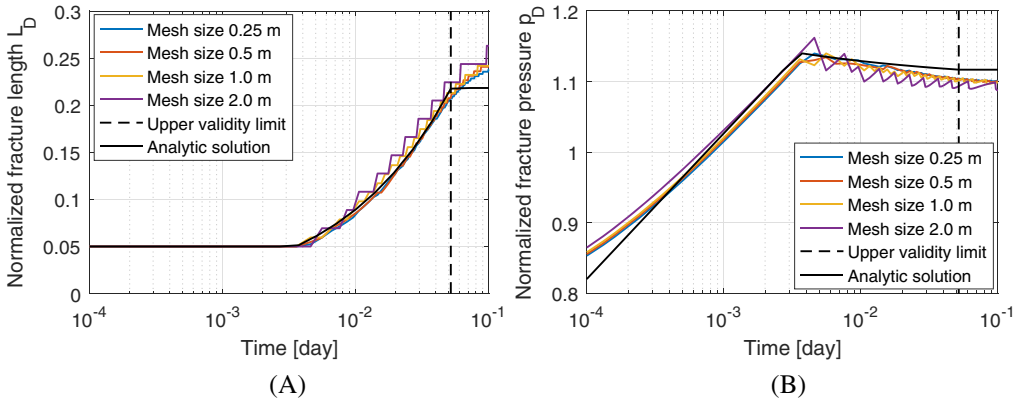

FIGURE 11 A, Fracture length comparison with a maximum time step equal to $1{\cdot}10^{-3}$ day. Increase of an average mesh size makes the numerical fracture outrun its analytical counterpart. Solutions obtained with the average mesh sizes of 0.25 and 0.5 m fit the analytical solution. B, Bottom hole pressure comparison. The curve for the larger mesh size exhibits higher pressure jumps upon opening of new fracture segments. Pressure curves corresponding to denser meshes demonstrate smoother behavior [Colour figure can be viewed at wileyonlinelibrary.com]

We plot the length of the fracture for different time steps in Figure 12(A). Small time steps match the analytical solution very well and bigger time steps lead to a delay in fracture growth. Irrespective of the time step used, all solutions yield the same final fracture length. In addition, irrespective of the chosen time step, all curves have the same rate increment during the active fracture growth.

Figure 12(B) shows variation of the bottom hole pressure for solutions obtained with different time steps. All the solutions exhibit similar height of fluctuations as they were obtained on the same mesh. However, the width of these fluctuations varies for different time steps. The use of a larger time step also leads to a slight underestimation of the bottom hole pressure during the initial stage of the pressure accumulation.

Analysis of both plots led to the conclusion that, to capture fracture growth accurately, the time step size should be sufficiently small. The absence of the evaluation points during the pressure growth stage may cause delays in length and pressure profiles. However, the differences in length are not significant and provide a reasonable approximation even at the largest time step used.

4.8 | Effect of the mesh irregularity

In the previous examples, the fracture is growing along the horizontal line, defined by the grid geometry. In the current subsection, we perform several tests where no such a predefined path exists. Fracture growth is stimulated in four geometries with different mesh sizes. They are 0.25, 0.5, 1.0, and 2.0 m. All the simulations are performed with an adaptive time step starting with $1{\cdot}10^{-5}$ day and ending with $5{\cdot}10^{-3}$day. Resulting fracture geometries are given in Figure 13. Development of the fracture length and bottom hole pressure is shown in Figure 14.

From the analysis of Figure 13, we see that for a denser mesh (red line), fracture trajectory is almost straight. For coarser meshes, the fracture paths' irregularity is more pronounced. However, in all the simulations, fractures are following the most straight paths possible. In Figure 14(A), the large mesh size (green line) has the larger deviation from the analytical solution. The rest of the mesh resolutions (0.2, 0.5, and 1.0 m) give solutions very close to the analytical curve. Bottom hole pressure change, given in Figure 14(B), leads to a similar conclusion. The bottom hole pressure has a larger error for a coarser mesh.

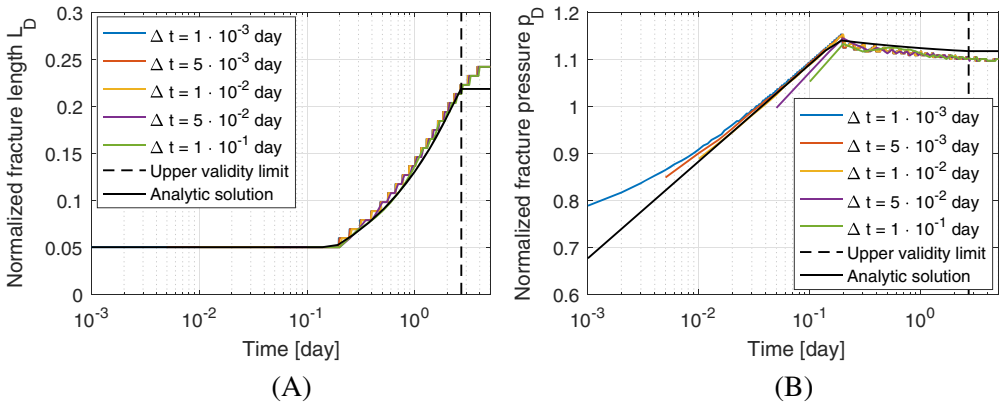

FIGURE 12 The normalized fracture length (A) and pressure comparison (B) in the time step refinement study for the model with an average mesh size equal to 0.5 m. An increase of the time step leads to a slight delay of the fracture growth. Irrespective of the time step size, the final fracture length and incremental rate are similar for all the simulations. The length and pressure curves obtained with the smallest time step size ($1{\cdot}10^{-3}$ day) have the best match with the analytical curve in its validity range [Colour figure can be viewed at wileyonlinelibrary.com]

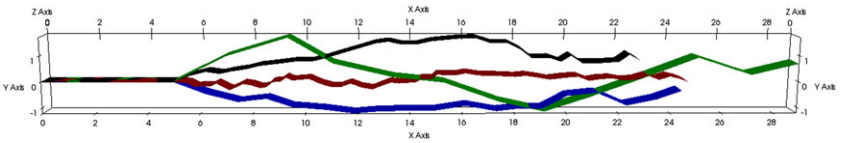

FIGURE 13 Fracture paths for geometries with no horizontal line in front of the initial fracture (resolutions: red line, 0.25 m; black line, 0.5 m; blue line, 1.0 m; and green line, 2.0 m) [Colour figure can be viewed at wileyonlinelibrary.com]

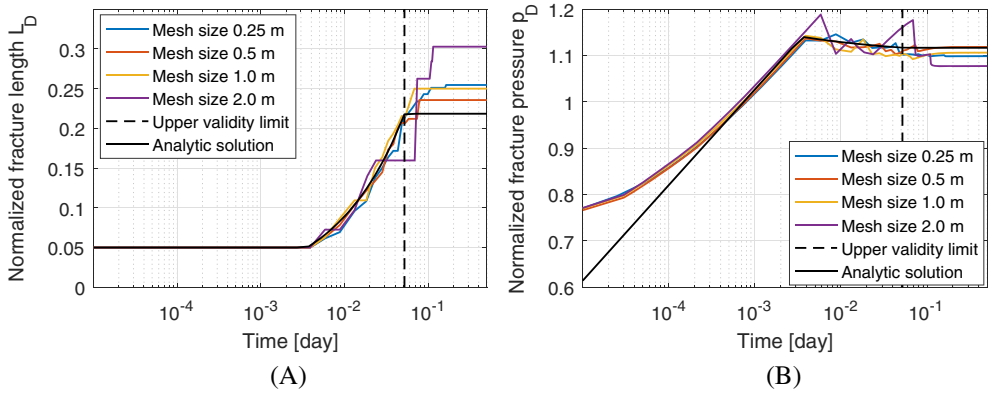

FIGURE 14 A, Comparison of the fracture lengths in time for meshes without a perfectly horizontal path. The largest mesh size shows an overshoot in length and nonsmooth growth in time. Denser meshes have better agreement with the analytical curve. B, Pressure development curves. A solution obtained on a larger mesh size exhibits higher pressure fluctuations upon opening of new segments [Colour figure can be viewed at wileyonlinelibrary.com]

The performed study demonstrates the applicability of the proposed algorithm for the class of problems with irregular unstructured grids. Additional tests including sensitivity to the initial fracture length, volume of inactive fracture elements, compressibility of the fluids, and turning fractures were conducted as well but are omitted here for brevity. Full description can be found in the MSc thesis by Gallyamov.[59]

5 | PRACTICAL APPLICATION

The purpose of this chapter is to demonstrate the applicability of the developed model to some practical tasks. The specific problem solved here is modeling hydraulic fracture growth during waterflooding operations within a classic injection pattern. The waterflooding operation aims to increase recovery of hydrocarbons by their displacement with injected water. Different injection patterns may be used. Here, we consider one of the most common ones - the inverted 9-spot. This injection pattern is a specific design of a reservoir development plan, where water is injected into a well surrounded by 8 producing wells. A schematic representation of the pattern is given in Figure 15(A). It is adopted in many oil & gas fields worldwide due to its high extraction rates and the coverage ratio.

An example of a successful use of 9 spots is the Priobskoye field in Western Siberia, Russia. The field is the second largest field by the amount of geological reserves in Russia, after the Samotlorskoye field. It has a low-permeability

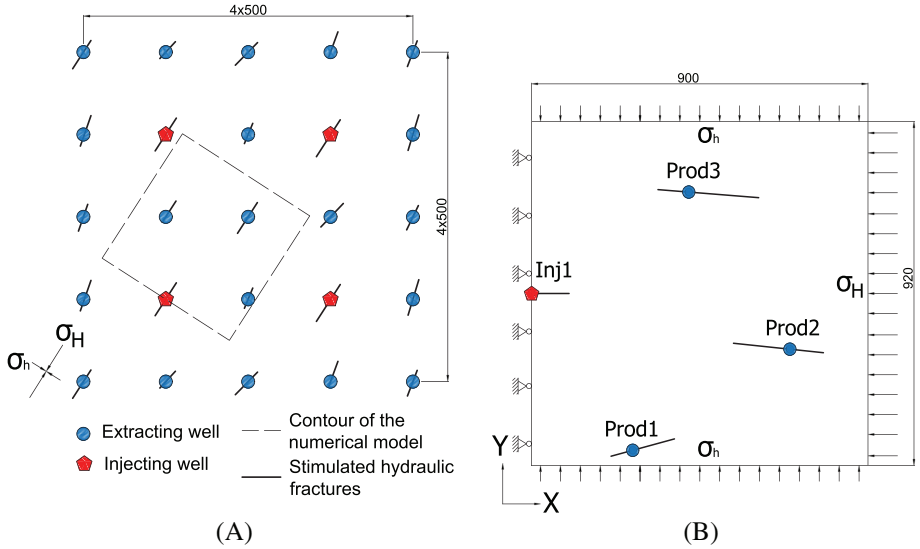

FIGURE 15 A, Inverted 9-spot injection pattern and direction of principal stresses. B, Simulated part of the pattern with the boundary conditions for the mechanical part [Colour figure can be viewed at wileyonlinelibrary.com]

porous matrix, and the hydraulic fracturing is widely used to accelerate the production. A typical stimulated fracture half-length is around 100 to 150 m. However, when the water injection process begins, the induced fractures continue to grow owing to waterflooding. The half-length of these extended fractures may reach 350 to 400 m. This can lead to an early water breakthrough at production wells. A comparison of well test results performed in the years 2004 and 2008 verified the assumption that water injection causes fracturing.[60] To illustrate the effect of the early water breakthrough and demonstrate growth of induced fractures, we consider the coupled geomechanical model for the following problem setup.

5.1 | Model description

Here, we model induced fracture behavior in the section of the injection pattern. The considered region is denoted by the dashed line (see Figure 15A). Because of the symmetry of the pattern, the modeled section comprises one injecting and three producing wells. Induced hydraulic fractures are oriented in the direction perpendicular to the minimum horizontal stress σ_h with a small deviation of $\pm 8°$. The length of the induced fractures is approximately 200 to 300 m. To simplify generation of the model input, boundaries of the region are co-oriented with the direction of principal stresses. The considered domain and its boundary conditions for the mechanical problem are given in Figure 15(B). To reduce the size of the discrete model, only a half-space is modeled. The symmetrical boundary condition is imposed at $x = 0$ m. The computational domain is defined by Ω=[900×920×1m]. The mesh with an average size of an element equal to 10 m in the center and 100 m toward the boundaries is used. The matrix is discretized using 9990 prismatic elements and 10 052 vertices. The fractures are discretized using 11 695 rectangles. The total number of control volumes is 21 685.

Initial conditions for the mechanical part correspond to the stresses applied at the boundaries. The flow domain is surrounded by the impermeable boundaries. The fluid is injected at the rate of Q_{inj}. Recovery is ensured by extracting oil from three wells with the production rate of $Q_{ext}=Q_{inj}/3$ each. Since the model is 2-D and the numerical domain has a third dimension equal to 1 m, injection flow rates are given per unit height of the reservoir, and the used unit of cubic meter per day corresponds to each meter of the reservoir thickness. The conductivity of the fracture segments is sensitive to the stress field. Values corresponding to the Barnett Shale were adopted from Zhang et al.[61] They are shown as a function of the normal traction and the aperture in Figure 16. The curve on the left is plotted against the fracture aperture, while the right part is plotted against the normal traction acting on a fracture surface. The reduction of the stresses on the fracture surface and following opening of the fracture leads to increase in its conductivity. Properties of the reservoir, injected and extracted fluids and the operational parameters are given in Table 4.

5.2 | Results

We consider two typical waterflooding scenarios. The first one is characterized by the absence of induced fracture when the injection flow rate is relatively low. The second one is induction of the fracture growth by injection of water at a high rate. Even for the noninduced fracture case, including the geomechanical calculation makes a

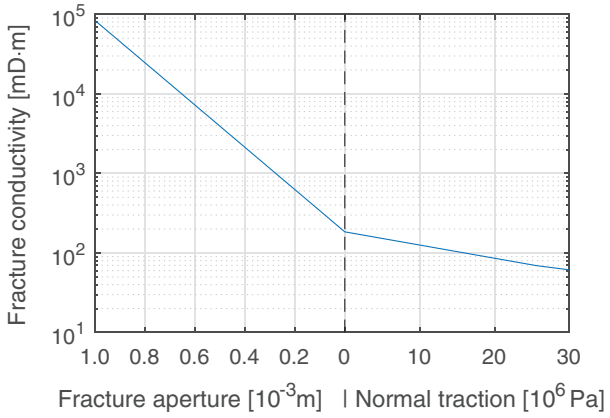

FIGURE 16 Fracture conductivity as a function of its aperture (left) and normal traction (right) [Colour figure can be viewed at wileyonlinelibrary.com]

TABLE 4 Parameters used in numerical simulations

Property	Value
Porosity ϕ	0.2
Permeability k, mD	5
Density ρ_s, kg/m^3	2500
Biot coefficient α	1
Young modulus E, GPa	20
Poisson ratio ν	0.25
Rock compressibility C_r, 1/Pa	$1{\cdot}10^{-10}$
Fracture toughness K_{Ic}, Pa$\sqrt{\text{m}}$	$30{\cdot}10^{5}$
Oil density ρ_o, kg/m^3	1000
Water density ρ_w, kg/m^3	1000
Oil viscosity μ_o, cP	0.5
Water viscosity μ_w, cP	0.2
Oil compressibility $C_{p,o}$, 1/Pa	$5{\cdot}10^{-10}$
Water compressibility $C_{p,w}$, 1/Pa	$4{\cdot}10^{-10}$
Endpoint relative permeability of oil k_{ro}	0.8
Endpoint relative permeability of water k_{rw}	0.8
Mobility ratio M	2.5
Initial reservoir pressure p_{init}, MPa	20.0
Stress in the X direction σ_H, MPa	−38.6
Stress in the Y direction σ_h, MPa	−36.0
Initial oil saturation s_o	0.75
Initial water saturation s_w	0.25
Irreducible oil saturation s_{oi}	0.1

significant impact on the results. It allows predicting conductivity changes of fractures and a porous medium owing to change of stresses.

The nonpropagating fracture response was observed in the numerical simulations with water injection rates of Q_{inj}=5, 7, and 9 m^3/day. The resulting pressure and water saturation profiles after three years of injection of Q_{inj}=9 m^3/day are shown in Figure 17. Pressure growth along the hydraulic fracture connected to the injection well is much more pronounced than the pressure drop in producers. The reason behind this phenomenon is the aperture-dependent fracture conductivity. As the injection well tends to open up the fracture, its conductivity increases. In contrast, production wells reduce the pressure in their surroundings, which leads to an increase of the normal traction. As a result, conductivity of fractures at producing wells reduces. The waterfront, explicitly visible in Figure 17(B), still does not reach any of the producing wells after three years.

Different waterflooding responses, with growing hydraulic fracture, were observed in simulations with injection rates of Q_{inj}=14, 21, and 28 m^3/day. Pressure and water saturation profiles for simulation with Q_{inj}=21 m^3/day after three years are shown in Figure 18. In comparison with the previous case, pressure and water saturation fronts advanced on a larger distance owing to a conductive path, created by the fracture, and the higher value of the injection rate. It can also be seen that the waterfront reaches all producing wells.

Bottom hole pressure, normalized over the minimum horizontal stress σ_h, is given in Figure 19(A). To compare typical behavior irrespective of time, the variables are plotted against the volume of injected water normalized by the drained pore volume, V_{injw}/V_{por}. The ratio V_{injw}/V_{por} shows the fraction of the available pore volume already displaced by water and serves as an indicator of waterflooding progress. Pressure curves for nongrowing fractures (5, 7, and 9 m^3/day) stay below similar curves for growing fracture cases (14, 21, and 28 m^3/day) throughout the whole simulation time. The critical pressure value, after which the fracture starts growing, is found in between these two sets. In the growing

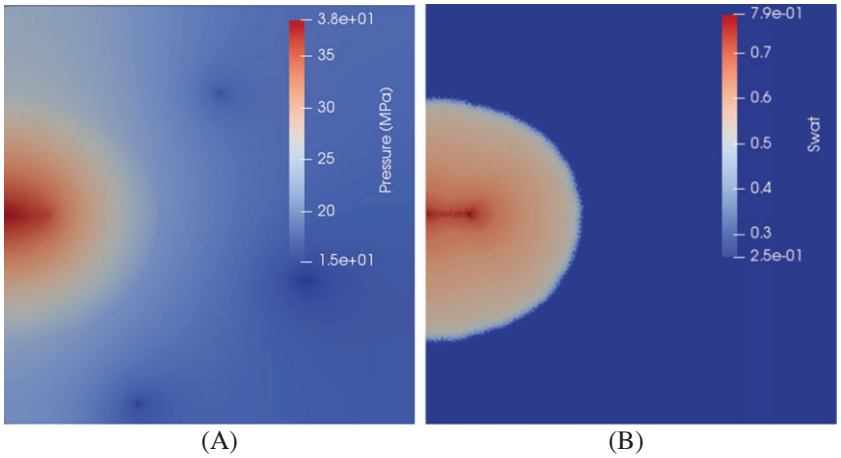

FIGURE 17 Pressure (A) and water saturation (B) profiles across the domain in the simulation with Q_{inj}=9 m^3/day after 3 years. No pronounced water break at the producing wells is observed [Colour figure can be viewed at wileyonlinelibrary.com]

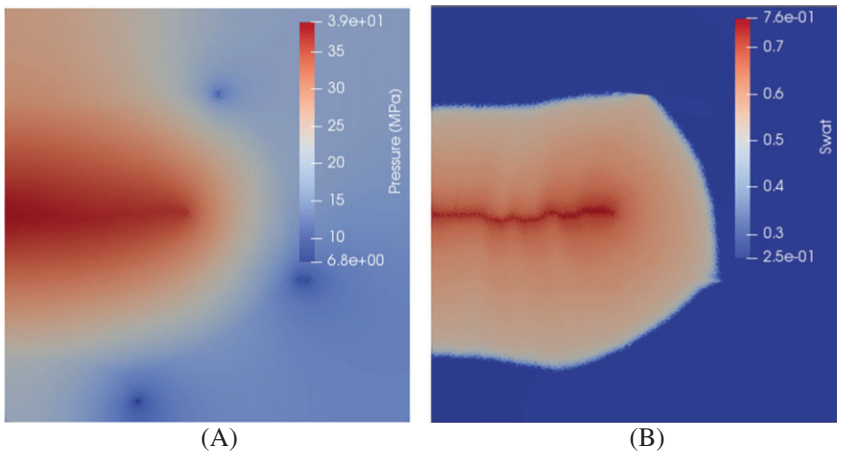

FIGURE 18 Pressure (A) and water saturation (B) profiles across the domain in the simulation with Q_{inj}=21 m^3/day after 3 years. Water front, larger owing to the extended fracture, reaches producing wells causing water break through [Colour figure can be viewed at wileyonlinelibrary.com]

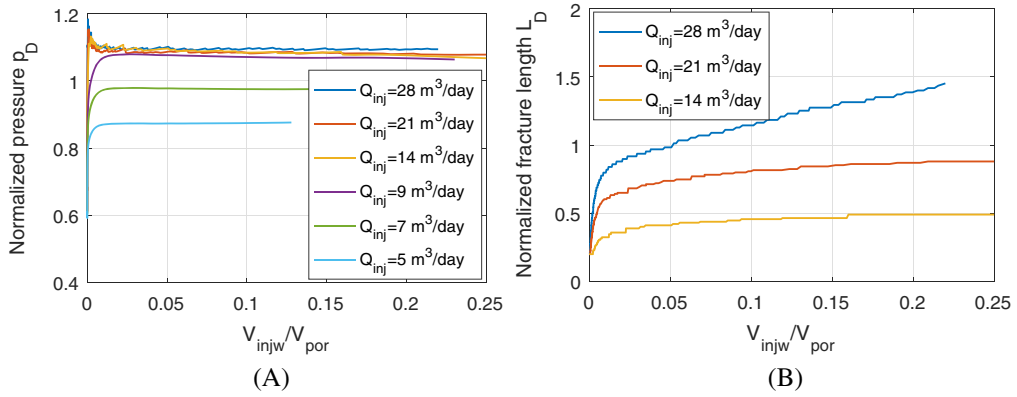

FIGURE 19 A, Bottom hole pressure at the injector normalized by minimum horizontal stress, p_D=BHP/σ_h, against the volume of the injected water normalized by the displaceable pore volume, V_{injw}/V_{por}. B, Fracture length normalized by minimum distance between two wells, L_D=L/W, against the volume of injected water normalized by the displaceable pore volume, V_{injw}/V_{por} [Colour figure can be viewed at wileyonlinelibrary.com]

fracture cases, pressure increases above the critical stress, which makes fracture propagation possible. Unlike the non-growing fracture case, the pressure profile for the growing fracture case has fluctuations associated with opening of new fracture segments. The fracture with the initial length of 1/4W (W is the shortest distance between two neighboring wells) develops a length larger than W.

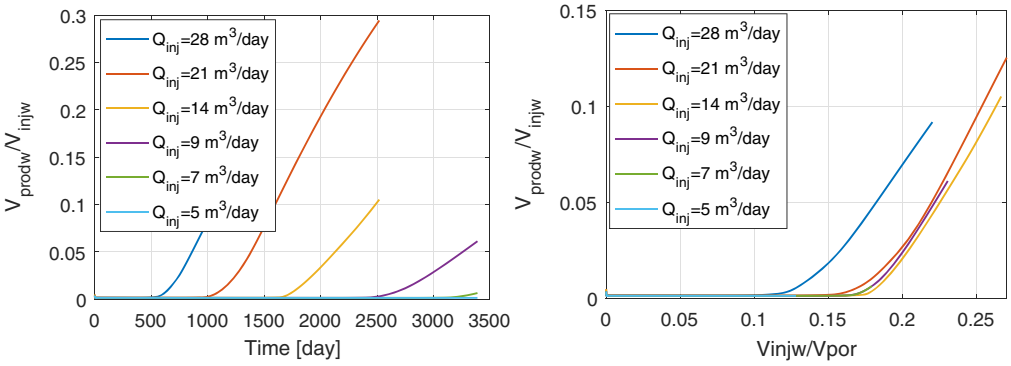

FIGURE 20 A, Produced water volume normalized by the volume of injected water, V_{prodw}/V_{injw}, against time. B, Same variable plotted against the volume of injected water normalized by the displaceable pore volume, V_{injw}/V_{por} [Colour figure can be viewed at wileyonlinelibrary.com]

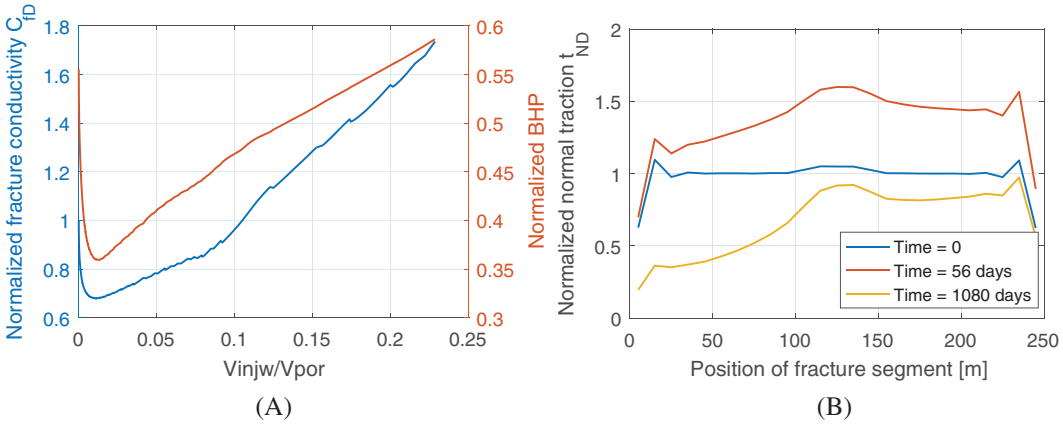

FIGURE 21 A, Conductivity of the fracture at the producing well Prod2 normalized over its initial conductivity, $C_{fD}=C_f/C_{f0}$, and evolution of the BHP at the Prod2 normalized over the minimum horizontal stress BHP/σ_h plotted versus the volume of injected water V_{injw}/V_{por}. B, A profile of the normal traction along the fracture normalized over the effective horizontal stress $t_{ND}=t_N/\sigma'_h$. The distance along the horizontal axis is given from the leftmost end of the fracture toward its rightmost end [Colour figure can be viewed at wileyonlinelibrary.com]

Fracture length changes for three simulations are shown in Figure 19(B). The figure reveals that the growth rate is directly dependent on the injection rate. Similarly to pressure behavior, the most intensive fracture growth happens during displacement of the first 2% of the total pore volume. Assessment of Figure 19(A,B) shows that, although the bottom hole pressure profiles at the injector are very similar during the fracture growth, the corresponding lengths are different. During the waterflooding operation, controlling only the injection pressure is not sufficient for having control over the induced fracture length.

Water production as a function of time is shown in Figure 20(A). Higher injection rates lead to an earlier water breakthrough. However, the efficiency of the waterflooding operation cannot be evaluated based on Figure 20(A). For this purpose, Figure 20(B) is introduced. It shows the volume of produced water with respect to the volume of injected water V_{prodw}/V_{injw}. When fracture is not induced, the water production curve is the same for all of the flow rates (5, 7, and 9 m^3/day). In contrast, the growing fracture changes the waterflooding performance. In this particular case, development of the hydraulic fracture with $Q_{inj}=14m^3$/day leads to a more effective operation and later water breakthrough than in the case with the nongrowing fracture. However, a further increase of the injection rate leads to an earlier water break.

Evolution of the fracture conductivity during the waterflooding process is given in Figure 21 and correlated with the pressure at the adjacent production well. The averaged conductivity of the fracture at the producing well Prod2 is normalized over its initial (undisturbed) conductivity, $C_{fD}=C_f/C_{f0}$, and plotted against the injected volume of water normalized over the pore volume. After 1% of the total pore volume is displaced ($V_{injw}/V_{por}=0.01$ or 56 days), the conductivity drops down to $0.7C_{f0}$ but further recovers and almost doubles. This behavior is caused by the initial pressure drop around the producing well followed by the pressure increase due to the arrival of the pressure signal from the injector.

The normal traction profile along the fracture surface is plotted in Figure 21. It is normalized over the effective minimum horizontal stress $t_{ND}=t_N/\sigma'_y$. Reduction of pressure leads to a higher normal traction on the fracture (see Figure 21(B) at time=56 days) and reduces its conductivity. Increase of pressure, in contrast, reduces the normal traction and lets the fluid flow faster within the fracture (see Figure 21(B) at time=1080 days).

As can be seen from the last example, dynamics of the induced fracture can significantly change the efficiency of the waterflooding operations. With limited fracture propagation, the sweep efficiency can be enhanced, which leads to a higher oil recovery factor. However, when the propagation is too fast, the efficiency drops because of faster water breakthrough to the production wells. This process is highly nonlinear and involves complex interactions between the propagating and existing fractures. In the presence of large uncertainties in reservoir properties, a fully coupled simulation of the entire process is extremely important to achieve a better production strategy.

6 | CONCLUDING REMARKS

A model that allows simulation of the fracture growth in the waterflooding process is proposed in this study. The model consists of the contact-enriched finite element method for mechanics and the finite-volume based Discrete Fracture Model approach for flow. To simulate the fracturing process, Irwin's fracturing criterion for linear elastic failure of mode I is adopted. Two methods of Stress Intensity Factor K_I estimation are implemented within the AD-GPRS framework. In the first approach, K_I is calculated using the Displacement Extrapolation Technique, where K_I values are extrapolated toward the fracture tip. In the second approach, the Virtual Crack Closure Technique is used as an alternative. Maximum tangential tensional effective stress values are used to determine a preferable fracture direction.

The solution algorithm involves simultaneous solution of the flow, energy, and mechanics equations. The Stress Intensity Factor is evaluated at each nonlinear step, and fracture trajectory is updated when K_I reaches the critical value. A fracture trajectory follows the existing faces of the computational grid. Only faces connected to a fracture tip can be activated or deactivated. Activated faces are added to the fracture trajectory. On the basis of the selected solution strategy, the face activation algorithm is performed on each nonlinear iteration. Alternatively, this strategy can be combined with other criteria for fracture propagation.

Several validation tests were performed where the results are compared against the available semianalytical solutions. The test cases include fracture propagation in a porous medium with single- or multi-phase fluids. Obtained results are in a full compliance with the analytical solution. Another test case is devoted to an injection of cold fluid into a hot reservoir. Cooling of the reservoir by injected water leads to the shrinkage of porous medium. Resulting tensional stresses around the initial fracture facilitate its further propagation. Comparison of the numerical and analytical results confirmed accuracy of the proposed model in capturing thermoelastic effects.

In addition, the proposed model was tested in a realistic field application. A segment of an inverted 9-spot injection pattern is simulated with different injection and production rates. Fracture growth rate and its final length show strong dependence on the injection rate. Limited fracture propagation may improve the efficiency of waterflooding operations. However, when propagation is too fast owing to the higher rate, efficiency may drop owing to faster breakthrough of water to production wells.

ACKNOWLEDGEMENT

We thank the Reservoir Simulation Industrial Affiliates Consortium at Stanford University (SUPRI-B) for providing access to the AD-GPRS.

ORCID

Emil Gallyamov http://orcid.org/0000-0002-2970-0890
Timur Garipov http://orcid.org/0000-0003-1805-6160

REFERENCES

1. Khristianovich S, Zheltov Y. Formation of vertical fractures by means of highly viscous fluids. In: Proc. 4th World Petroleum Congress; 1955; Rome, Italy:579-586.

2. Geertsma J, De Klerk F. A rapid method of predicting width and extent of hydraulically induced fractures. *J Pet Technol*. 1969;21(12): 1-571.
3. Perkins TK, Kern LR. Widths of hydraulic fractures. *J Pet Technol*. 1961;13(09):937-949.
4. Nordgren RP. Propagation of a vertical hydraulic fracture. *Soc Petrol Eng J*. 1972;12(04):306-314.
5. Hagoort J. Waterflood-induced hydraulic fracturing. *PhD thesis*. Delft, The Netherlands: Delft Technical University; 1981.
6. Koning E. Waterflooding under fracturing conditions. *PhD thesis*. Delft, The Netherlands: Delft Technical University; 1988.
7. Van Den Hoek PJ, Matsuura T, De Kroon M, Gheissary G. Simulation of produced water reinjection under fracturing conditions. *SPE Prod Facil*. 1999;14(3):166-176.
8. Hustedt B, Qiu Y, Zwarts D, Van Den Hoek PJ. Modeling water-injection-induced fractures in reservoir simulation. In: SPE Annual Technical Conference and Exhibition; 2005; Dallas, Texas:1323-1331.
9. Dikken BJ, Niko H. Waterflood-induced fractures: a simulation study of their propagation and effects on waterflood sweep efficiency. In: Society of Petroleum Engineers; 1987.
10. Granet S, Fabrie P, Lemonnier P, Quintard M. A two-phase flow simulation of a fractured reservoir using a new fissure element method. *J Pet Sci Eng*. 2001;32(1):35-52.
11. Monteagudo JEP, Firoozabadi A. Control-volume method for numerical simulation of two-phase immiscible flow in two-and three-dimensional discrete-fractured media. *Water Resour Res*. 2004;40(7).
12. Karimi-Fard M, Durlofsky LJ, Aziz K. An efficient discrete-fracture model applicable for general-purpose reservoir simulators. *SPE J*. 2004;9(2):227-236.
13. Juanes R, Samper J, Molinero J. A general and efficient formulation of fractures and boundary conditions in the finite element method. *Int J Numer Methods Eng*. 2002;54(12):1751-1774.
14. Kim J-G, Deo MD. Finite element, discrete-fracture model for multiphase flow in porous media. *AIChE J*. 2000;46(6):1120-1130.
15. Hoteit H, Firoozabadi A. An efficient numerical model for incompressible two-phase flow in fractured media. *Adv Water Resour*. 2008;31(6):891-905.
16. Martin V, Jaffré J, Roberts JE. Modeling fractures and barriers as interfaces for flow in porous media. *SIAM J Sci Comput*. 2005;26(5): 1667-1691.
17. Hoteit H, Firoozabadi A. Multicomponent fluid flow by discontinuous Galerkin and mixed methods in unfractured and fractured media. *Water Resour Res*. 2005;41(11):1-15.
18. Eikemo B, Lie K-A, Eigestad GT, Dahle HK. Discontinuous Galerkin methods for advective transport in single-continuum models of fractured media. *Adv Water Resour*. 2009;32(4):493-506.
19. Faivre M, Paul B, Golfier F, Giot R, Massin P, Colombo D. 2D coupled HM-XFEM modeling with cohesive zone model and applications to fluid-driven fracture network. *Eng Fract Mech*. 2016;159:115-143.
20. Nordbotten JM. Finite volume hydromechanical simulation in porous media. *Water Resour Res*. 2014;50(5):4379-4394.
21. McClure MW, Horne RN. Investigation of injection-induced seismicity using a coupled fluid flow and rate/state friction model. *Geophysics*. 2011;76(6):WC181-WC198.
22. Norbeck JH, McClure MW, Lo JoW, Horne RN. An embedded fracture modeling framework for simulation of hydraulic fracturing and shear stimulation. *Comput Geosci*. 2016;20(1):1-18.
23. Simo JC, Laursen TA. An augmented Lagrangian treatment of contact problems involving friction. *Comput Struct*. 1992;42(1):97-116.
24. Liu F, Borja RI. Stabilized low-order finite elements for frictional contact with the extended finite element method. *Comput Methods Appl Mech Eng*. 2010;199(37):2456-2471.
25. Gordeliy A, Peirce A. Coupling schemes for modeling hydraulic fracture propagation using the XFEM. *Comput Methods Appl Mech Eng*. 2013;253:305-322.
26. Puso MA, Laursen TA. A mortar segment-to-segment frictional contact method for large deformations. *Comput Methods Appl Mech Eng*. 2004;193(45):4891-4913.
27. Simo JC, Wriggers P, Taylor RL. A perturbed Lagrangian formulation for the finite element solution of contact problems. *Comput Methods Appl Mech Eng*. 1985;50(2):163-180.
28. Hansbo A, Hansbo P. An unfitted finite element method, based on Nitsche method, for elliptic interface problems. *Comput Methods Appl Mech Eng*. 2002;191(47):5537-5552.
29. Kachanov LM. *Introduction to Continuum Damage Mechanics*. Netherlands: Marinive Nijhoff; 1986.
30. Miehe C, Hofacker M, Welschinger F. A phase field model for rate-independent crack propagation: robust algorithmic implementation based on operator splits. *Comput Methods Appl Mech Eng*. 2010;199(45):2765-2778.
31. Miehe C, Welschinger F, Hofacker M. Thermodynamically consistent phase-field models of fracture: variational principles and multi-field FE implementations. *Int J Numer Methods Eng*. 2010;83(10):1273-1311.

32. Moës N, Stolz C, Bernard P-E, Chevaugeon N. A level set based model for damage growth: the thick level set approach. *Int J Numer Methods Eng*. 2011;86(3):358-380.
33. Bandis SC, Lumsden AC, Barton NR. Fundamentals of rock joint deformation. *Int J Rock Mech Min Sci and*. 1983;20(6):249-268.
34. Garipov TT, Karimi-Fard M, Tchelepi HA. Discrete fracture model for coupled flow and geomechanics. *Comput Geosci*. 2016;20(1):149-160.
35. AD-GPRS. Automatic Differentiation General Purpose Research Simulator; 2017.
36. Biot MA. Mechanics of deformation and acoustic propagation in porous media. *Jpn J Appl Phys*. 1962;33(4):1482-1498.
37. Coussy O. *Poromechanics*. Coussy. John Wiley & Sons; 2004.
38. Jaeger JC, Cook NGW, Zimmerman RW. *Fundamentals of Rock Mechanics*. 4th ed. 350 Main Street, Malden, MA 02148-5020, USA: Blackwell Publishing, Ltd; 2007.
39. Fu P, Johnson SM, Carrigan CR. An explicitly coupled hydro-geomechanical model for simulating hydraulic fracturing in arbitrary discrete fracture networks. *Int J Numer Anal Methods Geomech*. 2013;37(14):2278-2300.
40. Jha B, Juanes R. Coupled multiphase flow and poromechanics: a computational model of pore pressure effects on fault slip and earthquake triggering. *Water Resources Research*. 2014;50(5):3776-3808.
41. Barton C, Moos D, Tezuka K. Geomechanical wellbore imaging: implications for reservoir fracture permeability. *AAPG Bull*. 2009;93(11):1551-1569.
42. Irwin GR. Analysis of stresses and strains near the end of a crack traversing a plate. *J Appl Mech*. 1957;24:361-364.
43. Wriggers P, Laursen TA. Computational contact mechanics. *Wriggers*. Springer; Vol. 2. 2006.
44. Voskov DV. An extended natural variable formulation for compositional simulation based on tie-line parameterization. *Transp Porous Media*. 2012;92(3):541-557.
45. Garipov TT, Tomin P, Rin R, Voskov D, Tchelepi HA. Unified thermo-compositional-mechanical framework for reservoir simulation. *Comput Geosci*. 2018.
46. Terekhov KM, Mallison BT, Tchelepi HA. Cell-centered nonlinear finite-volume methods for the heterogeneous anisotropic diffusion problem. *J Comput Phys*. 2017;330:245-267.
47. Abushaikha AS, Voskov DV, Tchelepi HA. Fully implicit mixed-hybrid finite-element discretization for general purpose subsurface reservoir simulation. *J Comput Phys*. 2017;346:514-538.
48. Khait M, Voskov DV. Operator-based linearization for general purpose reservoir simulation. *J Petrol Sci Eng*. 2017;157:990-998.
49. Giannakopoulos AE. The return mapping method for the integration of friction constitutive relations. *Comput Struct*. 1989;32(1):157-167.
50. White JA. Anisotropic damage of rock joints during cyclic loading: constitutive framework and numerical integration. *Int J Numer Anal Methods Geomech*. 2014;38(10):1036-1057.
51. Fu P, Johnson SM, Settgast RR, Carrigan CR. Generalized displacement correlation method for estimating stress intensity factors. *Eng Fract Mech*. 2012;88:90-107.
52. Chan SK, Tuba IS, Wilson WK. On the finite element method in linear fracture mechanics. *Eng Fract Mech*. 1970;2(1):1-17.
53. Settgast RR, Fu P, Walsh SDC, White JA, Annavarapu C, Ryerson FJ. A fully coupled method for massively parallel simulation of hydraulically driven fractures in 3-dimensions. *Int J Numer Anal Methods Geomech*. 2017;41(5):627-653.
54. Krueger R. Virtual crack closure technique: history, approach, and applications. *Appl Mech Rev*. 2004;57(2):109-143.
55. Carrier B, Granet S. Numerical modeling of hydraulic fracture problem in permeable medium using cohesive zone model. *Eng Fract Mech*. 2012;79:312-328.
56. Salimzadeh S, Paluszny A, Zimmerman RW. Three-dimensional poroelastic effects during hydraulic fracturing in permeable rocks. *Int J Solids Struct*. 2017;108:153-163.
57. De Pater CJ, Desroches J, Groenenboom J, Weijers L. Physical and numerical modeling of hydraulic fracture closure. *SPE Prod Facil*. 1996;11(2):122-128.
58. Van Dam CJ, Romijn R. Analysis of hydraulic fracture closure in laboratory experiments. *SPE Prod Facil*. 2000;15(3):151-158.
59. Gallyamov E. Hydraulic fracture propagation model for porous media. *Master's Thesis*. The Netherlands: Delft University of Technology; 2017.
60. Davletbaev A, Baikov V, Ozkan E, et al. Multi-layer steady-state injection test with higher bottomhole pressure than the formation fracturing pressure. In: Society of Petroleum Engineers; 2010.
61. Zhang J, Kamenov A, Zhu D, Hill AD. Laboratory measurement of hydraulic fracture conductivities in the Barnett shale. In: IPTC 2013: International Petroleum Technology Conference; 2013.
62. Muskat M. *The Flow of Homogeneous Fluids Through Porous Media*. 1st ed. Ann Arbor, Michigan, USA: J. W. Edwards, Inc; 1946.
63. Perkins TK, Gonzalez JA. Effect of thermoelastic stresses on injection well fracturing. *Soc Pet Eng J*. 1985;25(1):78-88.

How to cite this article: Gallyamov E, Garipov T, Voskov D, Van den Hoek P. Discrete fracture model for simulating waterflooding processes under fracturing conditions. *Int J Numer Anal Methods Geomech*. 2018;42:1445–1470. https://doi.org/10.1002/nag.2797

APPENDIX A

SEMIANALYTICAL SOLUTION

The following semianalytical solution for fracture length is used. It consists of solutions for pressure and stresses and a fracture propagation criterion. The semianalytical solution for the pressure distribution was developed by Koning.[6] First, the elliptical coordinate system is used:

$$\begin{aligned} x &= L\cosh\xi\cos\eta, \\ x &= L\sinh\xi\sin\eta, \end{aligned} \tag{A1}$$

where L is the fracture length, ξ is the ellipse number starting from the smallest, and η is the direction angle. Further, a solution for the steady-state pressure profile surrounding an infinite conductivity fracture derived by Muskat[62] was used:

$$\Delta p(\xi) = \frac{Q\mu}{2\pi kh}\ln\left(\frac{a_e + b_e}{L} - \xi\right) \quad , \tag{A2}$$

where q is the injection flow, μ is the fluid viscosity, k is the absolute permeability, h is the fracture thickness, and a_e and b_e are the semiaxes of an area influenced by the change in pressure. It is assumed that the pressure penetration front moves radially outward with respect to the slowly growing fracture. This allows us to define an effective time-dependent exterior radius as follows:

$$R_e(t) = 1.5\sqrt{\eta t} \quad , \tag{A3}$$

where η is the fluid diffusivity. After Equation A3 is substituted into Equation A2, the following equation for pressure distribution in the late-time regime is obtained:

$$\Delta p(\xi) = \frac{Q\mu}{2\pi kh}\ln\left(\frac{3\sqrt{\eta t}}{L} - \xi\right) \quad . \tag{A4}$$

Koning[6] modified this equation to account for different fluid properties in three domains surrounding the fracture: (1) cold water zone, (2) warm water zone, and (3) oil zone. Pressure distribution in the near-fracture (cold water) zone is described in the following way:

$$p(\xi, t) = p_R + \frac{Q}{2\pi h}\left[\frac{1}{\lambda_c}\left(\ln\frac{a_c + b_c}{L} - \xi\right) + \frac{1}{\lambda_w}\ln\frac{a_w + b_w}{a_c + b_c} + \frac{1}{\lambda_{oil}}\ln\frac{3\sqrt{\eta_{oil} t}}{a_w + b_w}\right] \quad , \tag{A5}$$

where λ_c, λ_w, and λ_{oil} are the fluid mobilities for cold, warm, and oil zones, respectively, and a_i and b_i with i=c, w, oil are the major and minor semiaxes of these zones.

A simple analytical solution have been derived for the SIF from stresses at infinity is used. It is rewritten in terms of pressures and stresses:

$$p_f - \sigma_0 - \Delta\sigma_P - \Delta\sigma_T = \frac{K_{Ic}}{\sqrt{\pi L}} \quad , \tag{A6}$$

where p_f is the pressure inside the fracture, σ_0 is the far-field total stress perpendicular to the fracture face, $\Delta\sigma_P$ and $\Delta\sigma_T$ are the induced stresses on the fracture face caused by pressure and temperature changes in the vicinity of the fracture. Next, analytical solutions have been derived for the pressure- and temperature-induced stresses, which for the 2-D case can be written as

$$\Delta\sigma_{\mathrm{P}} = \frac{1}{2}A_{\mathrm{p}}[p(\xi=0)-p_R]-A_{\mathrm{p}}\frac{Q}{4\pi h}\frac{1}{\lambda_{\mathrm{c}}}\left[\frac{b_{\mathrm{c}}}{a_{\mathrm{c}}+b_{\mathrm{c}}}+\frac{\lambda_{\mathrm{c}}}{\lambda_{\mathrm{w}}}\left(\frac{b_{\mathrm{w}}}{a_{\mathrm{w}}+b_{\mathrm{w}}}-\frac{b_{\mathrm{c}}}{a_{\mathrm{c}}+b_{\mathrm{c}}}\right)+\frac{\lambda_{\mathrm{c}}}{\lambda_{\mathrm{oil}}}\left(\frac{1}{2}-\frac{b_f}{a_f+b_f}\right)\right], \tag{A7}$$

where A_{p} is the poroelastic constant, related to Biot coefficient α through $A_{\mathrm{p}}=\frac{1-2\nu}{1-\nu}\alpha$.

Expression for the pressure- and temperature-induced stresses is based on the study by Perkins and Gonzalez,[63] who proposed an empirical fit to numerical simulations:

$$\Delta\sigma_{\mathrm{T}} = A_{\mathrm{T}}(T_{\mathrm{c}}-T_{\mathrm{oil}})\left[\frac{b_{\mathrm{c}}}{a_{\mathrm{c}}+b_{\mathrm{c}}}+\frac{a_{\mathrm{c}}}{a_{\mathrm{c}}+b_{\mathrm{c}}}\cdot\frac{1}{1+1/2\cdot[1.45(h/2b_{\mathrm{c}})^{0.9}+0.35(h/2b_{\mathrm{c}})^{2}][1+(b_{\mathrm{c}}/a_{\mathrm{c}})^{0.774}]}\right], \tag{A8}$$

where A_{T} is the thermoelastic constant, related to the linear thermal expansion coefficient β through $A_{\mathrm{T}}=E\beta/(1-\nu)$. Equation A8 is based on the assumption of the elliptic shape of the fracture cross section. When this assumption is adopted for the 2-D scenario, fracture height h is taken equal to infinity. That makes the second term in the brackets to vanish. When obtaining Equation A8, authors ignored heat conduction, making heat convection the only energy flow mechanism. Equation A6 with Equations A5, A7, and A8 forms a set of semianalytical equations used for benchmarking of the developed numerical model.

APPENDIX B

NONLINEAR SOLUTION PROCEDURE

Algorithm 1 Solution procedure

Input: $\mathbf{R}_n = \left(p_n, T_n\right)$, $\mathbf{U}_n = \left(\boldsymbol{u}_n, t_{N,n}, t_{T,n}\right)$, $\Gamma_{f^a,n}$, $\Gamma_{f^p,n}$
  Set $k = 0$
  Set "Fracturing" = **true**, "Stabilization" = **false**
  Set $\mathbf{R}^k_{n+1} = \mathbf{R}_n$, $\mathbf{U}^k_{n+1} = \mathbf{U}_n$ and $\Gamma^k_{f^a} = \Gamma_{f^a,n}$
  Calculate initial error norms for mass and energy $\|\mathcal{R}_f\|$, and for momentum balance equations $\|\mathcal{R}_m\|$
  while $\left(\|\mathcal{R}_f\| \geq \varepsilon_f, \quad \|\mathcal{R}_m\| \geq \varepsilon_m\right)$ **do**
    Solve the mass, energy, and momentum balance equations for $\left(p^{k+1}_{n+1}, T^{k+1}_{n+1}, \boldsymbol{u}^{k+1}_{n+1}\right)$

    Detect opening and closing faces
    if (Tip face $\in \Gamma^k_{f^a,n+1}$) **then**
      Calculate SIF
      if ($K_I > K^*_I$ & "Fracturing" = **true**) **then**
        Project stress values and evaluate tensile forces on each face connected to the tip
        Select a face with a corresponding maximum tensile force
        Add face into $\Gamma^{k+1}_{f^a,n+1}$
        Change mesh numbering
      end if
      if ($K_I < 0$ & Tip $\notin \Gamma_{f^a,n}$) **then** ▷ Allow closure of faces activated on current time step only
        Subtract face from $\Gamma^{k+1}_{f^a,n+1}$
        Change mesh numbering
      end if
    end if
    Solution stabilization
    if (Stabilization option activated) **then**
      if $\left(\text{Length}\left(\Gamma^{k+1}_{f^a,n+1}\right) > \text{Length}\left(\Gamma^{k}_{f^a,n+1}\right)\right)$ **then**
        Set "Stabilization" = **true**
      end if
      if ("Stabilization" = **true**) **then**
        Check solution stabilization conditions: maximum iterations, residual norms, etc.
        if ("Stabilization" conditions satisfied) **then**
          Set "Stabilization" = **false**
        end if
      end if
      if ("Stabilization" = **true**) **then**
        Set "Fracturing" = **false** ▷ Do not allow opening of new segments
      else
        Set "Fracturing" = **true** ▷ Allow opening of new segments
      end if
    end if

    Evaluate contact integrals
    for all (Faces $\in \Gamma_{f^p}$) **do**
      Solve the system of equations equations (21e -21f)
      Update the traction values $t^{k+1}_{N,n+1}, t^{k+1}_{T,n+1}$
    end for
    Evaluate the contact integral Eq. 20

    Evaluate the residual norms
    if (Stabilization option activated) **then** ▷ Do not evaluate the norms during the stabilization step
      if ("Stabilization" = **false**) **then**
        Calculate the error norms for mass and energy $\|\mathcal{R}_f\|$, and for the momentum balance equations $\|\mathcal{R}_m\|$
      end if
    else
      Calculate the error norms for the mass and energy $\|\mathcal{R}_f\|$, and for the momentum balance equations $\|\mathcal{R}_m\|$
    end if
    Set $k = k + 1$
  end while
Output: $\mathbf{R}^k_{n+1}$, $\mathbf{U}^k_{n+1}$, and $\Gamma^k_{f^a,n+1}$
  Perform next timestep t_{n+1}